Chapter 6

Effect of the Absorber Morphology on the Solar Cell Performance

In this section, solar cells are presented in which the Spray ILGAR $CuInS_2$ thin films analyzed in the previous chapters served as absorber layers. As a basis for this study, this chapter starts with an introductory section about the basic properties and underlying physical principles of $CuInS_2$-based thin-film solar cells. Additionally, the current-density-voltage (*JV*) and quantum efficiency (*QE*) measurements, which were applied for the characterization of the devices, are briefly described (section 6.1.). In section 6.2., the Spray ILGAR $CuInS_2$-based solar cells are analyzed by *JV*- and *QE*-measurements, in order to understand the mechanisms that limit their efficiency. Based on the results of the Raman analysis in chapter 5, the photovoltaic performance of the devices is correlated to the influence of the *well-crystallized top layer* and the *layered bottom layer* (Fig. 3.13).

6.1. Solar Cells Based on $CuInS_2$

Generally, solar cells consist of p- and n-type semiconductors forming a pn-junction. In a pn-junction, a space charge is built up by the equilibrium of the competing diffusion (due to the different carrier concentrations in the p- and n-type regions) and drift (due to the electric field built up by carrier diffusion) currents across the junction [Würfel '05]. In thermal equilibrium, both currents cancel each other and lead to the implementation of the so-called space charge region (SCR).
If a flux of photons with energy hν exceeding the band gap energy E_{gap} of the absorbing semiconductor impinges on a pn-junction, the photons are absorbed and excite electrons from the valence band to the conduction band, thus creating electron-hole-pairs. In a single semiconductor, these electron-hole-pairs would recombine after a certain time under emission of a photon of the energy h$\nu = E_{gap}$. Due to the electric field in the SCR, electron-hole-pairs generated in the SCR, are separated by this field. After separation, the electrons and holes diffuse to the front and back contacts and can be utilized to drive an electric load.
In planar $CuInS_2$-based thin-film solar cells, the pn-junction is usually formed by a heterojunction of a p-type $CuInS_2$ *absorber layer* and a n-type ZnO *window layer*[26]. In order to improve the band alignment in this junction, a *buffer layer*, usually consisting of CdS, is deposited in between the $CuInS_2$ and the ZnO. In Fig. 6.1a, a schematic sketch of the structure

[26] The ZnO layer consists of a bilayer of about 100 nm intrinsic ZnO (i-ZnO) and about 400 nm Al-doped n-type ZnO (n^+-ZnO). This bilayer structure of the window layer yielded the best solar cell performance, even though the role of the i-ZnO layer is still under discussion. Presumably it is needed to reduce the creation of shunt paths between the front and back contacts [Dhere '06; Jahagirdar '06].

of a $CuInS_2$-based thin-film solar cell is depicted. The corresponding band diagram of such a heterojunction is shown in Fig. 6.1b.

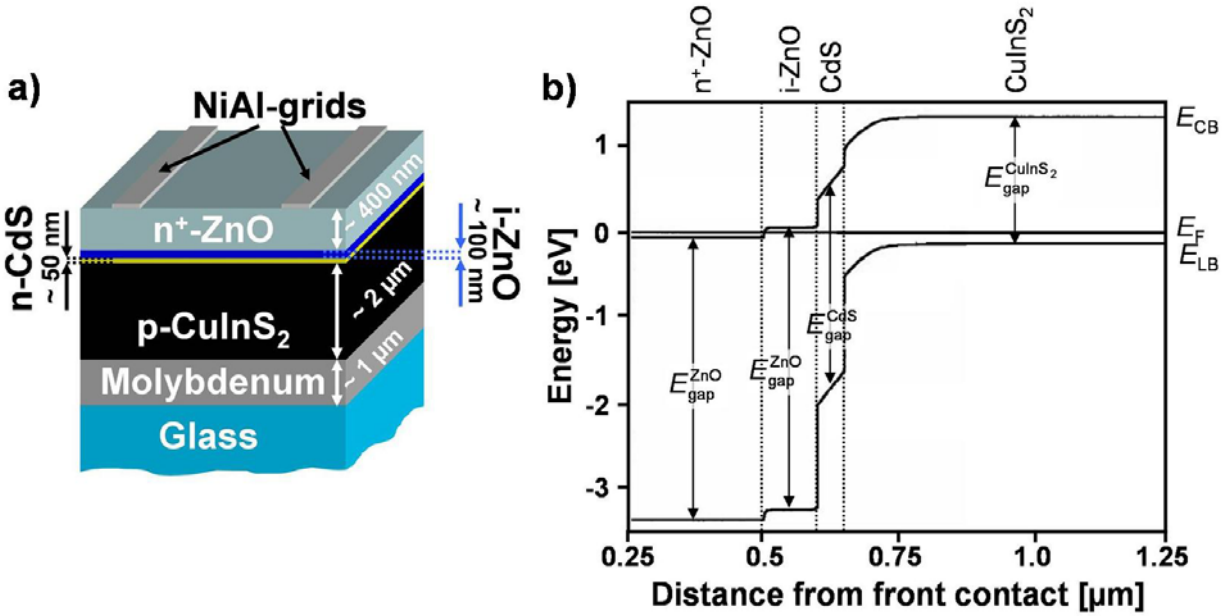

Fig. 6.1: a) Schematic sketch of the structure of a $CuInS_2$-based thin-film solar cell consisting of a layer sequence of glass/molybdenum/$CuInS_2$/CdS/i-ZnO/n^+-ZnO/NiAl. b) band diagram of the $CuInS_2$/CdS/i-ZnO/n^+-ZnO heterojunction in such a device. The diagram was adapted from Ref. [Klenk '01].

Such devices consist of a stack of layers of the sequence glass/molybdenum/$CuInS_2$/CdS/i-ZnO/n^+-ZnO/Ni-Al. Standard soda-lime glass of 2-3 mm thickness is used as a substrate. The molybdenum back contact has a thickness of about 1 µm. The $CuInS_2$ absorber layer is about 2-3 µm thick, followed by a 50 nm CdS, a 100 nm i-ZnO and a 400 nm n^+-ZnO layer, which complete the pn-junction. For laboratory scale devices, NiAl-grids are deposited on top of the n^+-ZnO layer, in order to facilitate the contacting of the devices. In order to avoid the creation of shunt paths between the front and back contact of the device, the layers need to exhibit a compact morphology without voids. Additionally, for the absorber layer, a grain size of 1-2 µm is beneficial, since grain boundaries are potential recombination centers, which could cause a loss of generated charge carriers and thus lead to a decrease of the solar cell efficiency [Gloeckler '05].

Incident light enters this structure from the ZnO-side. As it travels through the solar cell structure, the light is absorbed by the various materials depending on its wavelength and on the thickness of the respective layer. Within a medium of absorption coefficient $\alpha_{abs}(\lambda)$, the intensity of an incident beam of light of wavelength λ decreases with increasing depth from its initial value $I_0(\lambda)$ according to the law of Lambert-Beer:

$$I(d,\lambda) = I_0(\lambda) \cdot \exp\left(-\alpha_{abs}(\lambda) \cdot d\right) \qquad \text{Eq. (6.1)}$$

ZnO has an optical band gap of 3.3 eV. Consequently, $\alpha_{abs}(\lambda)$ strongly increases for photons with an energy $h\nu$>3.3 eV, so that almost all of these photons are absorbed by the n^+-ZnO (400 nm) and i-ZnO (100 nm) layers. Photons of lower energy are partially absorbed by the CdS layer, which has a band gap of 2.4 eV. However, due to its limited thickness (50 nm) only about 5 % of the incident photons are absorbed by this layer. Due to its direct band gap of 1.5 eV and its high absorption coefficient (about 10^5 cm^{-1} for $h\nu$>1.5 eV [Neumann '81]), most of the remaining light with $h\nu$>1.5 eV is absorbed in the $CuInS_2$ absorber layer.

Current Density-Voltage Dependence of $CuInS_2$-Based Solar Cells

If a voltage is applied to a pn-junction, the charge transport across the junction can be described by the diode-equation [Shockley '49]. In an illuminated pn-junction, i.e. an illuminated solar cell, the electron-hole-pairs generated by the incident photons, constitute additional charge carriers and cause an additional current density J_{photo}, which - in first approximation - is constant and superimposed onto the current density of the diode. In the *one-diode model*, an illuminated solar cell is represented by the equivalent circuit in Fig. 6.2.

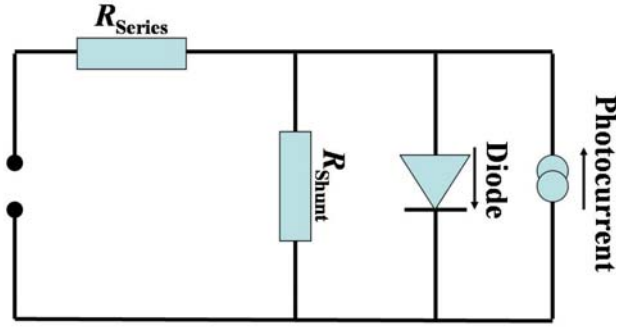

Fig. 6.2: Equivalent circuit of a solar cell according to the one-diode-model [Würfel '05].

The equivalent circuit consists of the diode, a series resistance R_{Series}, a parallel or shunt resistance R_{Shunt} and an additional parallel current density, which is opposed to the diode current density. For an ideal solar cell, R_{Series} equals zero and R_{Shunt} is infinite. The current density-voltage (JV) dependence of the equivalent circuit in Fig. 6.2 can be described by a generalized diode equation [Rau '99]:

$$J(V) = J_0 \cdot \left[\exp\left(\frac{\mathrm{e} \cdot \left(V - R_{\mathrm{Series}} \cdot J \right)}{A \cdot \mathrm{k_B} \cdot T} \right) - 1 \right] + \frac{V - R_{\mathrm{Series}} \cdot J}{R_{\mathrm{Shunt}}} - J_{\mathrm{photo}} \qquad \text{Eq. (6.2)}$$

Here, $\mathrm{e} \approx 1.602 \cdot 10^{-19}$ C is the elementary charge, $\mathrm{k_B} \approx 1.038 \cdot 10^{-23}$ J/K the Boltzmann constant and A is the so-called *diode quality factor*. The *saturation current density* J_0 is given as:

$$J_0 = J_{00} \cdot \exp\left(\frac{-E_{\mathrm{A}}}{A \mathrm{k_B} T} \right) \text{ and becomes } J_0 = J_{00} \cdot \exp\left(\frac{-E_{\mathrm{gap}}}{\mathrm{k_B} T} \right) \text{ for an ideal diode} \qquad \text{Eq. (6.3)}$$

The *reference saturation current density* J_{00} also shows a weak temperature dependence [Rau '99]. In Eq. (6.3), E_A is the activation energy of the saturation current density. In an ideal diode, E_A is equal to the band gap energy and $A = 1$. The values for E_A and A in real solar cells are determined by the predominant recombination mechanisms. In a first approximation, J_{photo} can be assumed to be independent of the voltage V.

It has been shown that for $CuInS_2$-based thin-film solar cells the recombination of charge carriers in the space charge region is the dominating recombination mechanism so that other mechanisms can be neglected [Hengel '00; Ito '00; Reiss '02]. Therefore, the approximation of the current density-voltage dependence of these devices by the one-diode-model (Eq. (6.2)) is sufficient and will be used for the analysis of the Spray ILGAR $CuInS_2$-based solar cells in this chapter.

In Fig. 6.3a, the JV-curves as obtained in the dark and under standardized AM 1.5 illumination[27] of a $CuInS_2$-based solar cell are shown. In Fig. 6.3a, parameters commonly used to characterize a solar cell are also shown:

[27] The standardized air mass (AM) 1.5 solar spectrum (100 mW/cm^2) is shown and described in Appendix IX.

- The open circuit voltage V_{OC} is the voltage for which the current density across the junction becomes zero, i.e. $J(V_{OC}) = 0$ mA/cm^2.
- The short circuit current density J_{SC} is the current density across the junction for $V = 0$ V, i.e., $J(0) = J_{SC}$.
- The fill factor FF describes the shape of the JV-curve. It can be calculated from the area ratio of the two rectangles in Fig. 6.3a: The area of the dashed rectangle corresponds to the maximum power that can be extracted out of the solar cell, $P_{max} = V_{max} \cdot J_{max}$. The area of the gray rectangle ($V_{OC} \cdot J_{SC}$) corresponds to the upper limit for P_{max} for a JV-curve of rectangular shape.

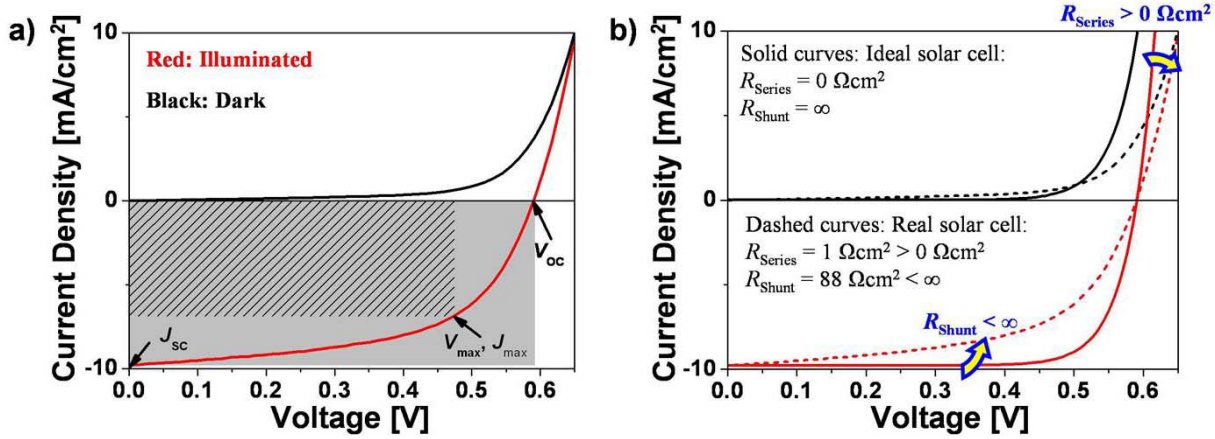

Fig. 6.3: a) JV-curves of a $CuInS_2$-based solar cell in the dark (black) and under AM 1.5 [NREL '08] illumination (red). The dashed rectangle corresponds to the maximum power $P_{max} = V_{max} \cdot J_{max}$ that can be extracted from the cell, whereas the gray rectangle describes the upper limit ($V_{OC} \cdot J_{SC}$) for P_{max} for a cell with $FF = 100\%$. In b) the influence of a non-zero series resistance R_{Series} and a finite shunt resistance R_{Shunt} on the JV-curves of a solar cell is shown.

From these parameters and the incident power P_{in} of the illuminating light (100 mW/cm^2 for AM 1.5 illumination, Appendix IX), the efficiency η of a solar cell can be calculated according to Eq. (6.4). It yields the ratio of the incident power and the maximum power which can be extracted out of the solar cell.

$$\eta = \frac{FF \cdot J_{SC} \cdot V_{OC}}{P_{in}} = \frac{P_{max}}{P_{in}} \qquad \text{Eq. (6.4)}$$

In Fig. 6.3b, the influence of a non-zero series resistance R_{Series} and a finite shunt resistance R_{Shunt} on the JV-curve of a solar cell is shown. The solid curves correspond to the JV-curves of an ideal solar cell (Eq. (6.1)) for $R_{Series} = 0$ Ωcm^2 and $R_{Shunt} = \infty$, whilst the dashed curves were obtained from a Spray ILGAR $CuInS_2$-based solar cell. As R_{Series} increases and R_{Shunt} decreases, the JV-curve flattens, which corresponds to a decreasing fill factor. A non-zero R_{Series} is due to the non-zero resistance of the layers and contacts in the cell, whereas a finite value for R_{Shunt} is caused by shunt paths between the front and back contacts of the device that bypass the pn-junction. The effects of R_{Series} and R_{Shunt} on the JV-curve of solar cells are negligible (*relative* change of efficiency is smaller than 5 %) for R_{Series}<0.5 Ωcm^2 and R_{Shunt}>1000 Ω cm^2.
The photovoltaic parameters for an ideal $CuInS_2$-based solar cell without any recombination has been calculated by Blieske *et al.* for AM 1.5 illumination (Appendix IX) [Blieske '97]. These parameters are listed in Table 6.1 together with the parameters obtained from the best $CuInS_2$-based solar cell prepared to date [Siemer '01].

Table 6.1: Photovoltaic parameters for an ideal $CuInS_2$-based solar cell as calculated by Blieske *et al.* [Blieske '97] under AM 1.5 illumination and for the best $CuInS_2$-based solar cell reported to date by Siemer *et al.* [Siemer '01]. The difference between the active and total area efficiency is due to the shading effect of the NiAl grids in laboratory scale devices.

	Ideal $CuInS_2$ solar cell [Blieske '97]	Best $CuInS_2$ solar cell [Siemer '01]
J_{SC} [mA/cm^2]	27.1	24.3
V_{OC} [mV]	1249	729.4
FF [%]	90.1	71.7
η [%]	30.5	12.7 (active area); 11.4 (total area)

From the theoretical values, the potential of $CuInS_2$-based solar cells becomes clear. This potential is due to the band gap of 1.5 eV of $CuInS_2$, which ideally matches the solar spectrum [Henry '80]. In real devices based on $CuInS_2$, a maximum efficiency of 11.4 % was obtained by Siemer *et al.* [Siemer '01; Unold '06]. The strong deviation between the theoretical values and those obtained in real devices to date is presumably due to an unfavorable band alignment at the $CuInS_2$/CdS interface in these devices, which leads to an enhanced recombination rate at this interface [Klenk '01; Turcu '02]. For a further discussion of these recombination mechanisms the reader is referred to Ref. [Hengel '00; Ito '00; Reiss '02].

Quantum Efficiency of $CuInS_2$-Based Solar Cells

The quantum efficiency (QE) of a solar cell is defined as the ratio of the number of incident photons and the number of electrons extracted out of the device:

$$QE(\lambda) = \frac{e \cdot J_{photo}(\lambda)}{\Phi(\lambda)} = \frac{\text{Number of extracted electrons}(\lambda)}{\text{Number of incident photons}(\lambda)} \qquad \text{Eq. (6.5)}$$

Here, $\Phi(\lambda)$ is the photon flux of the incident light. Ideally, the QE of a solar cell would equal 100 % independently of the energy of the incident photons, i.e. every photon that impinges on the solar cell, would create an electron-hole-pair, which would be collected at an efficiency of 100 %. Obviously, this will not be the case in a real device, due to a non-zero recombination rate of the electron-hole-pairs and the presence of materials of different finite band gap energies in the device. Therefore, the QE of a solar cell deviates from the ideal value of 100 % in different spectral ranges for various regions. These deviations are summarized in Fig 6.4 and are discussed in the following.

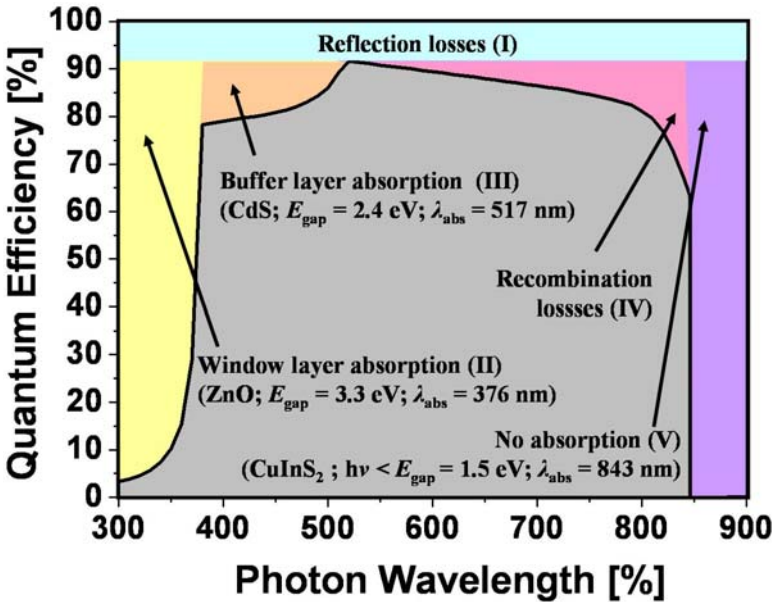

Fig. 6.4: Schematic QE-curve of a $CuInS_2$-based solar cell (black). The gray-shaded area below the curve represents the photons that led to the creation of electron-hole-pairs, which contributed to the photo-current of the device. The colored areas I-V represent the various types of losses that lead to the deviation of the QE from its ideal value of 100 %. These losses are discussed in the text.

- The first loss mechanism that leads to a *QE* below 100 % is the reflection of incident light at the surface of the solar cell (I in Fig. 6.4). For the sake of simplicity, also the effect of partial shading of the solar cell by the contact grids is included in region I. The percentage of the reflected light depends on its wavelength, but has been observed to be in the range of 5-10 % over the spectral range relevant for $CuInS_2$-based solar cells [Fuertes-Marron '03]. Therefore, the reflection losses are indicated as a constant loss in Fig. 6.4. If a measured *QE* curve is corrected for the reflection losses, it is referred to as *internal QE*, whereas the uncorrected curve is referred to as *external QE*. In this thesis only external *QE*-curves are discussed.
- The regions II and III in Fig. 6.4, corresponds to photons that are absorbed by the ZnO layers and by the CdS buffer layer. Since the SCR in $CuInS_2$-based solar cells is almost completely restricted to the $CuInS_2$-side of the pn-junction, these electron-hole-pairs generated in the ZnO and in the CdS are not collected and thus do not contribute to the photocurrent of the device.
- Region IV in Fig. 6.4 accounts for recombination and collection losses of electron-hole pairs in the absorber layer or at the absorber-buffer interface. These losses are most important for the analysis of the solar cell, since they depend on the actual quality of the device. In particular, the *QE*-curve reveals the wavelength dependence of the losses. Since the wavelength determines the penetration depth of the photons (Eq. (6.1)), conclusions about the depth-dependence recombination may be drawn.
- The losses in region V in Fig. 6.4 represent the photons whose energy hν lies below the optical band gap energy of $CuInS_2$. Hence, these photons cannot generate electron-hole-pairs in $CuInS_2$-based solar cells and do not contribute to the photocurrent of the device.

Since the *QE* represents the ratio of incident photons and extracted electrons, the short circuit current J_{SC} of a solar cell can be calculated from its measured *QE* by a convolution with the photon flux of the AM 1.5 solar spectrum $\Phi_{AM1.5}$ (Appendix IX):

$$J_{SC} = e \cdot \int_{\lambda} \Phi_{AM1.5} \cdot QE(\lambda) d\lambda \qquad \text{Eq. (6.6)}$$

Here, $e \approx 1.602 \cdot 10^{-19}$ C is the elementary charge. Eq. (6.6) provides a complementary method to determine J_{SC}. In particular, the probed area of the solar cell in *QE*-measurements is about 1 mm^2, whereas in *JV*-measurements the entire cell (50 mm^2) is illuminated. This allows the detection of local variations in J_{SC} on the mm-scale.
For a further discussion of *QE*-measurements, the reader is referred to Ref. [Vögt '92; Hegedus '04] and the references therein.

6.2. Spray ILGAR $CuInS_2$/CdS/i-ZnO/n^+-ZnO Heterojunctions

In this section, solar cells based on Spray ILGAR $CuInS_2$ absorber layers are analyzed. Thereby, a special emphasis is laid on the investigation of the influence of the absorber morphology on the photovoltaic performance of the device. In particular, the role of the *well-crystallized top layer* and of the *layered bottom layer* of the films is discussed.

On the one hand, the high density of crystallographic defects in the *layered bottom layer* of the Spray ILGAR $CuInS_2$ thin films (Fig. 3.13) can be expected to be detrimental for the efficiency of solar cells, if these films are used as absorber layers in such devices, since these defects may act as recombination centers for generated charge carriers [Schock '01]. Furthermore, the influence of the carbon-interlayers (Fig. 5.18) is not yet clear. On the other hand, it has to be taken into account that due to the high absorption coefficient of $CuInS_2$ (about 10^5 cm^{-1} for $h\nu > E_{gap}$, Fig. 6.9b) most of the absorbed light in a $CuInS_2$ thin-film solar

cell is absorbed in the first 100-300 nm of the absorber layer. It is this region, in which the Spray ILGAR $CuInS_2$ absorber films exhibit the largest grain sizes of up to several hundred nanometers. Therefore, it is not yet clear, how the bilayered morphology of Spray ILGAR $CuInS_2$ absorber layers will influence the photovoltaic performance of the solar cells based on such absorbers. This influence is analyzed in the following.

In this section, solar cells prepared from four different Spray ILGAR $CuInS_2$ thin films (samples 601-604) are discussed, which were prepared using the process described in section 3.3.2. The preparation parameters of these films are listed in Appendix I. These parameters were chosen based on the results of the growth mechanism analysis in chapter 4 in order to analyze the influence of the *well-crystallized top* and *layered bottom layer* of the Spray ILGAR $CuInS_2$ absorber layers on the performance of the solar cells. Samples 601-603 were deposited using parameters, which were found to result in a *well-crystallized top layer* of minimum thickness (compare sample 418; Table 4.2, Fig 5.13), whilst the parameters used for sample 604 resulted in a *well-crystallized top layer* of maximum thickness (compare sample 421; Fig. 4.18). The actual thickness of the *well-crystallized top layer* d_{TL} and the *layered bottom layer* d_{BL} for each film was determined from cross-sectional SEM images of the films by averaging over the thickness values obtained at 100 positions of the cross-sections. The nominal film thickness[28] was varied between 1.5 µm and 2.5 µm in order to assess its influence on the photovoltaic performance of the device and on the thickness of the *well-crystallized top layer* and the *layered bottom layer*. After deposition, the absorber layers were completed to solar cells according to the baseline process for $CuInS_2$-based thin-film solar cells described in section 2.2. [Klaer '03; Klenk '05]. All completed solar cells had a glass/Mo/$CuInS_2$/CdS/i-ZnO/n^+-ZnO/NiAl structure. After completion, each sample was structured by mechanical scribing, so that eight solar cells (0.5x1 cm^2) were obtained from one film.

In Table 6.2, the nominal absorber thickness and the thickness of the *well-crystallized top layer* d_{TL} and the *layered bottom layer* d_{BL} are listed for samples 601-604 together with the photovoltaic parameters of the solar cells. Fig. 6.5a-d show the *JV*-curves of the best solar cell of each sample together with a SEM image of the cross-section of the respective device.

Table 6.2: Properties of Spray ILGAR $CuInS_2$-based solar cells (samples 601-604): Nominal thickness d_{nom}, thicknesses of the *well-crystallized top layer* d_{TL} and of the *layered bottom layer* d_{BL} of the absorber layer. The uncertainties of d_{TL} and d_{BL} are the standard deviations of the values obtained from cross-sectional SEM images. The uncertainty of the nominal thickness, which follows from the XRF measurements (Appendix VII.iii), is ± 15 % (relative). The photovoltaic parameters (η, V_{OC}, J_{SC}, *FF,*) are given for the best cell and the average of the six best cells (out of eight) of every sample. The latter values were chosen to exclude scribing-related damages. R_{Series} and R_{Shunt} were obtained by fitting the *JV*-curves according to the one-diode-model (Eq. (6.2)) using the CurVA 2.0 software [Gloeckler_2 '05]. Their uncertainties reflect the uncertainties of the fits. Since not all curves could be described by the one-diode-model, R_{Series} and R_{Shunt} are only given for the best cell of each sample. All preparation parameters of the films are listed in Appendix I.

Sample		601	602	603	604
Nominal absorber thickness d_{nom} [nm]		1500	2000	2500	1700
Thickness of *well-crystallized top layer* d_{TL} [nm]		178 ± 88	289 ± 198	465 ± 173	461 ± 335
Thickness of *layered bottom layer* d_{BL} [nm]		1493 ± 134	2163 ± 218	2601 ± 495	1966 ± 490
η [%]	**best cell** / *Ave. best six*	**3.3** / *2.8*	**4.1** / *3.2*	**1.1** / *0.6*	**1.9** / *1.6*
V_{OC} [mV]	**best cell** / *Ave. best six*	**590** / *566*	**569** / *504*	**375** / *204*	**321** / *340*
J_{SC} [mA/cm^2]	**best cell** / *Ave. best six*	**9.8** / *9.1*	**16.3** / *13.2*	**11.8** / *11.6*	**18.9** / *14.0*
FF [%]	**best cell** / *Ave. best six*	**57.2** / *53.4*	**43.8** / *43.8*	**26.6** / *25.6*	**30.8** / *34.3*
R_{Series} [Ωcm^2]	**best cell**	**1.3 ± 0.1**	**1.0 ± 0.2**	**0.2 ± 0.1**	**0.8 ± 0.1**
R_{Shunt} [Ωcm^2]	**best cell**	**403 ± 12**	**88 ± 6**	**33 ± 3**	**19 ± 3**

[28] The nominal film thickness follows from the deposition rate of 30 nm/ILGAR-cycle determined by XRF for the deposition parameters of samples 601-603 (Table 4.3; sample 418). For the deposition parameters of sample 604, a deposition rate of 28 nm/ILGAR-cycle was determined (sample 421; in section 4.4.2.5.).

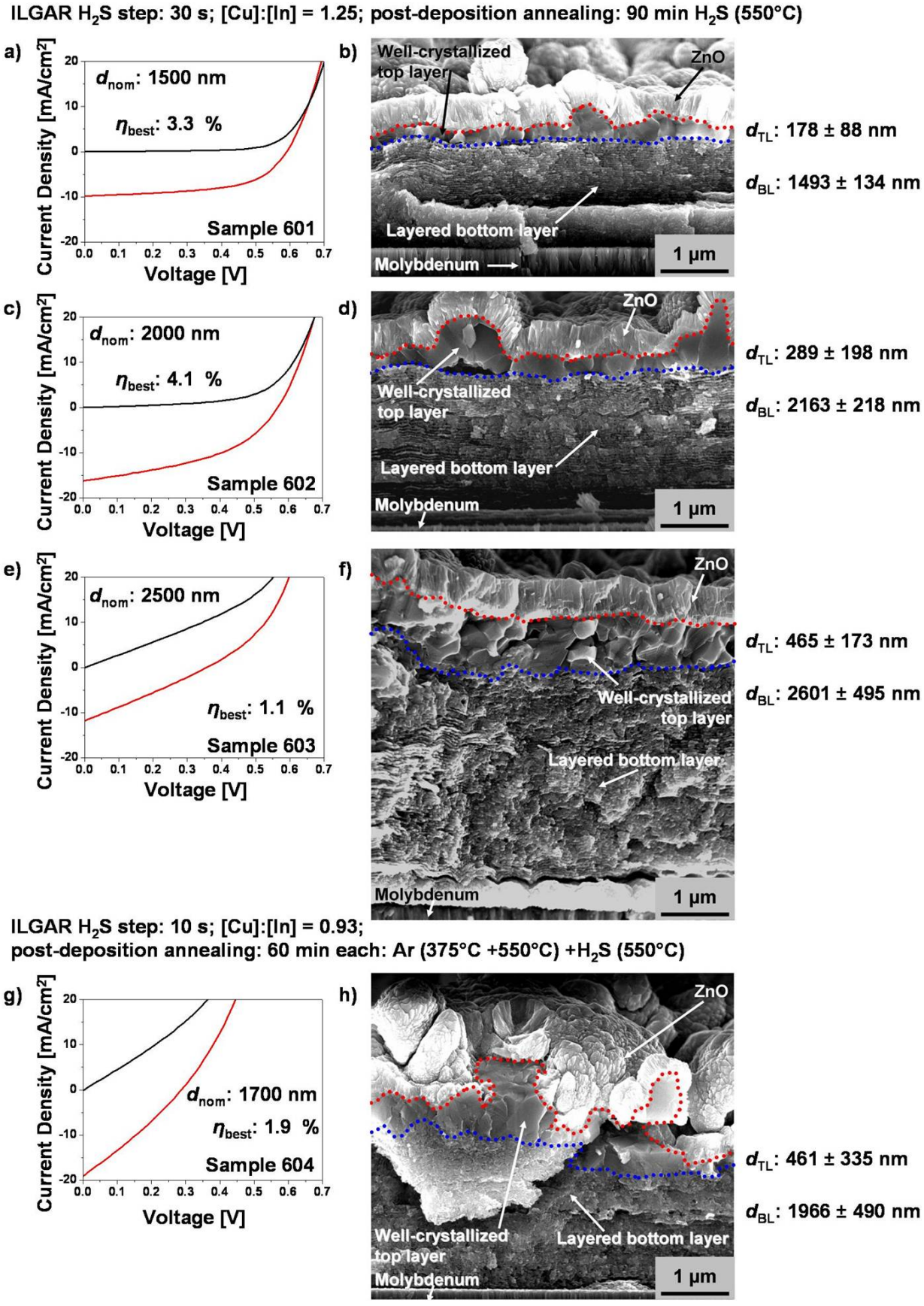

Fig. 6.5: Illuminated (red) and dark (black) *JV*-curves of the best solar cell of each of the samples 601-604 (a, c, e, g) and SEM images of the solar cell cross-sections of the same samples (b, d, f, h). The red dotted line in the SEM images marks the interfaces between the *well-crystallized top layer* and the window layer of the solar cell, whilst the blue dotted line marks the interface between the *well-crystallized top layer* and the *layered bottom layer*. The preparation parameters are listed in Appendix I.

The Spray ILGAR $CuInS_2$-based solar cells yield efficiencies of up to 4.1 % (sample 602). Even though the efficiencies listed in Table 6.2 are below those reported for the best $CuInS_2$-based vacuum-prepared solar cells of about 11 % [Siemer '01; Unold '06] (Table 6.1), these results show that working solar cells can be prepared from the Spray ILGAR $CuInS_2$ thin films. In the following, these results are interpreted with respect to the influences of the *well-crystallized top* and the *layered bottom layer* of the Spray ILGAR $CuInS_2$ films on the solar cell performance. Firstly, the morphological properties of the absorber layers are discussed and subsequently correlated to the photovoltaic parameters of the respective solar cells.

Morphology of the Spray ILGAR $CuInS_2$ Absorber Layers

The SEM images in Fig. 6.5 show that all films exhibited the expected bilayered morphology consisting of a *well-crystallized top layer* and a *layered bottom layer*, which was also observed for the thinner films in chapters 3 and 4. Even though the thickness of the *well-crystallized top layer* and the *layered bottom layer* showed fluctuations of up to 80 % (Table 6.2), the *top layer* was closed for all solar cells investigated in this section. This was different for the thinner films investigated in chapters 3 and 4, for which the parameters used for the preparation of samples 601-603, did not result in a closed *top layer* (sample 418, Fig. 5.13f). According to the growth model presented in chapter 4, this is a consequence of the larger amount of material used for the deposition of samples 601-603, which led to the formation of thicker *top layers* during the post-deposition H_2S annealing. The parameters used for the deposition of sample 604 already resulted in the formation of a closed *top layer* for thinner films (sample 421, Fig. 4.18e, f), which was also the case for the solar cell in this chapter.
In Fig. 6.6, the thicknesses of the *well-crystallized top layer* d_{TL} and the *layered bottom layer* d_{BL} is shown as functions of the nominal absorber thickness. For samples 601-603, the thicknesses of both layers seem to increase linearly with the nominal absorber thickness. Thereby, the thickness of the *bottom layer* approximately equals the nominal absorber thickness, which agrees with the growth model (section 4.5.). The *top* and *bottom layer* thicknesses of sample 604 agree with these linear dependences within their margin of uncertainty. However, the mean value of the *top layer* thickness of 461 nm in sample 604 exceeds the thickness of 235 nm, which follows from the linear fit of samples 601-603, by almost a factor of two. This indicates that the preparation conditions used for sample 604 led to an increased thickness of the *well-crystallized top layer* as it was concluded from the experiments in section 4.4.2.5.

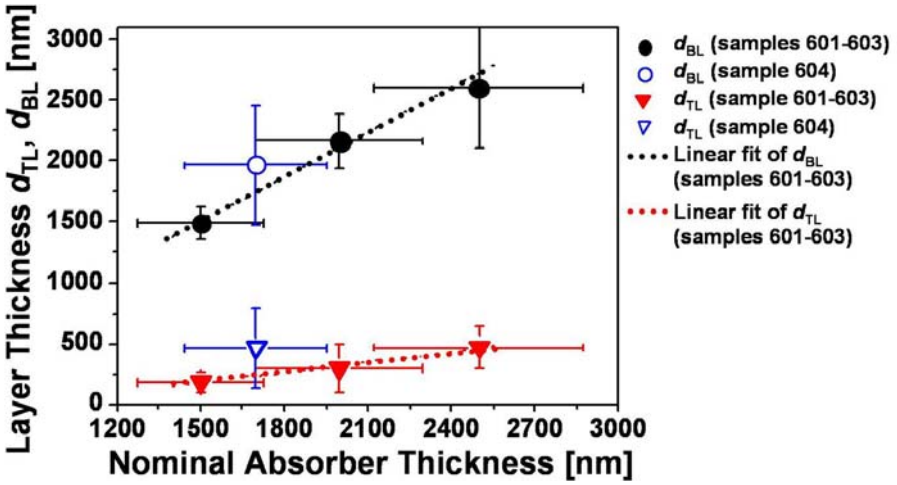

Fig. 6.6: Dependence of the thickness of the *well-crystallized top layer* and of the *layered bottom layer* of the Spray ILGAR $CuInS_2$ absorber layers on the nominal absorber layer thickness of samples 601-604 as determined from cross-sectional SEM images (Table 6.2; Fig. 6.5). The preparation parameters of the samples are listed in Appendix I.

Thus, the thicknesses of the *well-crystallized top layer* and the *layered bottom layer* of the solar cell absorbers behaved as expected from the model for the growth of the Spray ILGAR $CuInS_2$ films (section 4.5.). Hence, the influence of the *top* and *bottom layer* on the device performance can be discussed on the basis of this model in the following.

Influence of the Absorber Morphology on the Device Performance

The structural properties of the *well-crystallized top layer* (large grain size, single-phase chalcopyrite-type $CuInS_2$ composition), appear to be favorable for its photovoltaic application, whereas the properties of the *layered bottom layer* (nanocrystalline morphology, phase mixture of chalcopyrite-type and CuAu-ordered $CuInS_2$, carbon-contamination) can be expected to be unfavorable (chapter 5). Therefore, one may expect that a maximum thickness of the *well-crystallized top layer* and a minimum thickness of the *layered bottom layer* resulted in an optimum device performance. However, the parameters in Table 6.2 show that the opposite is the case: The solar cells obtained from samples 603 and 604 with *well-crystallized top layers* of maximum thickness of about 460 nm, showed the lowest efficiencies of the devices investigated in this section. Also the values for the open-circuit-voltage V_{OC} and for the fill factor *FF* were smaller than those obtained from samples 601 and 602.
The highest values for *FF* (57.2 %) and V_{OC} (590 mV) were obtained for sample 601 (Fig. 6.5a, b), which had the lowest *top* and *bottom layer* thickness of d_{TL} = 178 ± 88 nm and d_{BL} = 1493 ± 134 nm. However, the short-circuit-current-densities J_{SC} (9.8 mA/cm^2) of this film were the lowest. This indicates that the crystalline properties of this film are favorable for photovoltaics (high V_{OC} and *FF*), but the *top layer* thickness may be too small, so that not enough charge carriers can be generated (low J_{SC}). An increase of the thickness of the *well-crystallized top layer* (289 ± 198 nm) and of the *layered bottom layer* (2163 ± 218 nm) resulted in an increase of J_{SC} (16.3 mA/cm^2) and η (4.1 %), but led to a decrease of *FF* (43.8 %) and V_{OC} (569 mV) for sample 602. However, a further increase of the *top* and *bottom layer* thickness (sample 603: d_{TL} = 465 ± 173 nm; d_{BL} = 2602 ± 495 nm) did not lead to a further increase of J_{SC}, but to a decrease of all photovoltaic parameters compared to sample 602 (J_{SC} = 11.8 mA/cm^2, η = 1.1 %; *FF* = 26.6 %; V_{OC} = 375 mV). Also the preparation conditions chosen for sample 604 in order to obtain a *well-crystallized top layer* of maximum thickness, did not result in an increase of the efficiency, even though a maximum value for J_{SC} of 18.9 mA/cm^2 was obtained from the cells of this sample. These results show that the thickness of the *well-crystallized top layer* is not the only parameter that determines the device performance of the solar cells. The parameters in Table 6.2 indicate a dependence of the shunt resistance R_{Shunt} on the thickness ratio of the *layered bottom layer* and the *well-crystallized top layer*. In Fig. 6.7, the inverse shunt resistance of the best solar cells of samples 601-604 is shown as a function of the ratio of the average *bottom* and *top layer* thickness.

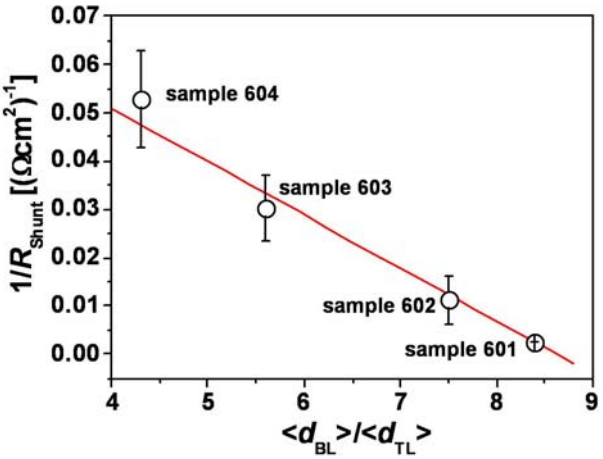

Fig. 6.7: Dependence of the inverse shunt resistance on the average thickness ratio of the *layered bottom layer* and the *well-crystallized top layer* for the best solar cells obtained from samples 601-604. The values for the series resistance were obtained by fitting the *JV*-curves of the solar cells according to the one-diode-equation (Eq. (6.2)) using the CurVA 2.0 software [Gloeckler_2 '05]. The red solid line is a linear fit of the data.

Fig. 6.7 indicates that R_{Shunt} depends inversely on this ratio. Also the *JV*-curves of the devices reflect the increasing shunt resistance for the best cells of samples 601-604 (Fig. 6.5). Whilst the *JV*-curve of the best cell of sample 601 ($<d_{BL}>/<d_{TL}>$ = 8.4; R_{Shunt} = 403 ± 12 Ωcm^2; Fig. 6.5a) showed an almost rectangular shape, the *JV*-curve of sample 604 ($<d_{BL}>/<d_{TL}>$ = 4.3; R_{Shunt} = 19 ± 3 Ωcm^2; Fig. 6.5g) was superimposed by a linear, i.e. ohmic, contribution of the photocurrent (compare also Fig. 6.3b). The *JV*-curves of the best cells of samples 602 and 603 showed a behavior in between these two cases (Fig. 6.5c, e). All solar cells investigated in this section had shunt resistances R_{Shunt} smaller than those of highly efficient $CuInS_2$-based solar cells (usually above 500 Ωcm^2 [Klaer '08]), whereas the series resistance R_{Series} was in a similar range as for such devices (1-2 Ωcm^2 [Klaer '08]).
A possible explanation for the observed dependence of the shunt resistance may be deduced from the growth model of the Spray ILGAR $CuInS_2$ absorber layers (section 4.5.). This model explained the formation of the *well-crystallized top layer* by the diffusion of indium out of the *layered bottom layer* into $Cu_{2-x}S$ agglomerates on the surface of the *layered bottom layer* during the post-deposition H_2S annealing (Fig. 4.20). Consequently, the average thickness ratio of the *bottom* and *top layer* $<d_{BL}>/<d_{TL}>$ reflects the amount of material which diffused out of the *bottom layer*. As indium diffuses out of the *bottom layer*, the porosity of the *bottom layer* increases. This can be assumed to have two effects on the shunt resistance:

- An increased porosity of the *bottom layer* favors the formation of cracks in the *bottom layer*, which may create shunt paths between the back and front contacts of the device. Such cracks were observed in the SEM investigations of sample 604, which showed the lowest $<d_{BL}>/<d_{TL}>$ ratio of 4.3. The risk of shunting is particularly high if the thickness of the *well-crystallized top layer* shows pronounced fluctuations, as it is the case in the Spray ILGAR $CuInS_2$ absorber layers (Table 6.2).
- As indium diffuses out of the *bottom layer*, previously formed $CuInS_2$ and the carbon interlayers consisting of a blend of (nanocrystalline graphite and amorphous carbon; section 5.3.) remain in the *bottom layer*. The more indium diffuses out, the less $CuInS_2$ will remain in the *bottom layer* (section 4.4.2.5.). Based on literature values for the conductivity of $CuInS_2$ (σ_{con} = 10^{-1}-10^{-5} Ω^{-1}cm^{-1} [Scheer '97]) and amorphous carbon (σ_{con} = 1-16 Ω^{-1}cm^{-1} [Rebollo-Plata '05]) it can be assumed that the outdiffusion of indium increases the risk that shunt paths between the front and back contacts are formed by the carbon interlayers.

Thus, even though the increased grain size in the *well-crystallized top layer* of the Spray ILGAR $CuInS_2$ absorber layers can be assumed to be favorable for the photovoltaic performance of the solar cells, its formation seems to increase the risk of forming shunt paths in the *layered bottom layer*, which cause a degradation of the device. Therefore, an increased diffusion of indium out of the *bottom layer*, which results in a decreased $<d_{BL}>/<d_{TL}>$, is expected to cause a decrease of the shunt resistance as it is observed in Fig. 6.7.

Photocurrent Contribution of the Well-Crystallized Top Layer and the Layered Bottom Layer

In the following, the contribution of the *well-crystallized top layer* and the *layered bottom layer* to the photocurrent of the solar cells are studied by wavelength-dependent *QE*-measurements. The wavelength of the photons impinging on a solar cell determine their penetration depth in the solar cell (Eq. (6.1)). Therefore, wavelength-dependent *QE*-measurements also reveal information about the depth-dependent contribution of the different absorber regions to the photocurrent of the device. In order to understand the influence of the bilayered morphology of the Spray ILGAR $CuInS_2$ absorber layer, *QE*-curves were calculated numerically for a $CuInS_2$/CdS/ZnO solar cell using the SCAPS software [Burgelman '00]. The assumed structure of the modeled solar cell is depicted schematically in Fig. 6.8a. Thereby, the absorber layer was assumed to consist of a "defect-poor" *top layer* of thickness d_{TL} and a

"defect-rich" *bottom layer* of thickness d_{BL} whose thicknesses were each varied between 1900 nm and 100 nm, such that the total absorber thickness remained at a constant value of 2 µm. The input parameters are given in Appendix IIX. The defect density and recombination rates of the "defect-poor" *top layer* corresponded to values used by Klenk to describe highly efficient $CuInS_2$-based solar cells numerically [Klenk '01]. For the "defect-rich" *bottom layer*, the recombination cross section of the defects was increased by two orders of magnitude (Appendix IIX). Note that the defect densities and recombination rates of both layers did not correspond to the real values in the *well-crystallized top layer* and the *layered bottom layer* of the Spray ILGAR $CuInS_2$ absorber layers, which are unknown. Therefore, the modeled *QE*-curves cannot be expected to describe the measured *QE*-curves quantitatively. However, the modeled *QE*-curves should qualitatively reflect the influence of a variation of the *top* and *bottom layer* thickness on the *QE*-curves of a solar cell. The calculated *QE*-curves are shown in Fig. 6.8b and c.

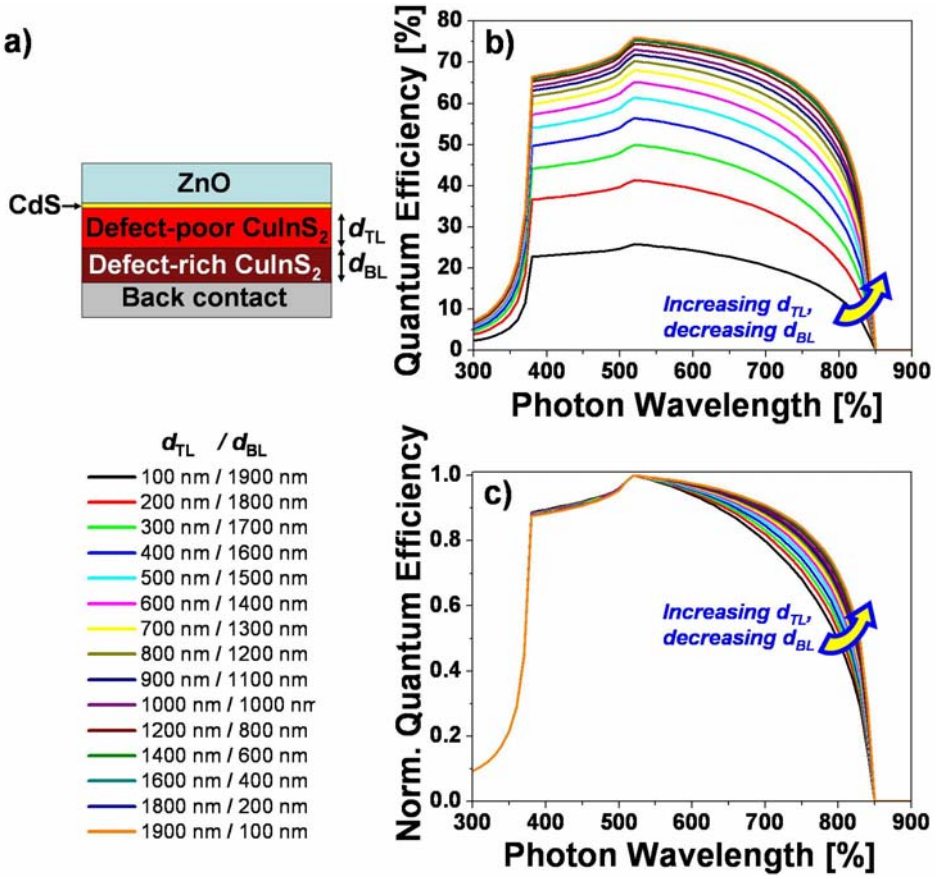

Fig. 6.8: Numerical simulations of *QE*-curves of a $CuInS_2$/CdS/ZnO solar cell with an absorber layer consisting of a defect-poor *top layer* of thickness d_{TL} and a defect-rich *bottom layer* of thickness d_{BL}. The *QE*-curves were calculated using the SCAPS software written by Burgelman *et al.* [Burgelman '00]. The input parameters of the simulations are given in Appendix IIX. a) Sketch of the solar cell structure of the simulated solar cells. b) Simulated *QE*-curves for the solar cell structure in a). d_{TL} and d_{BL} were each varied between 1900 nm and 100 nm keeping the total thickness constant at 2 µm. c) *QE*-curves from b) normalized to their maximum value.

From Fig. 6.8, two effects of the variation of d_{BL} and d_{TL} become apparent. Firstly, the increase of the *bottom layer* thickness d_{BL} at the expense of the *top layer* thickness d_{TL} leads to a decrease of the *QE* over the complete wavelength range of 300-850 nm (Fig. 6.8b). This is due to the fact that only the electron-hole pairs generated by photons in the defect-poor *top layer* contribute to the photocurrent. Since the penetration-depth increases for photons with increasing wavelength, the decrease of the *QE* for increasing *bottom layer* thickness is more

pronounced in the long wavelength region of the *QE*. This second effect can be seen from the normalized *QE*-curves in Fig. 6.8b.
In order to investigate the influence of the bilayered morphology of Spray ILGAR $CuInS_2$ absorber layers on the *QE* of the devices, *QE*-curves were recorded at four different spots on a solar cell of sample 601. Since this sample had the smallest *top layer* thickness (178 ± 88 nm) and the highest values for *FF* and V_{OC} of all investigated devices, the effects of the bilayered morphology on the *QE* can be expected to be most pronounced for this absorber layer.
In Fig. 6.9a, four *QE*-curves are shown, which have been recorded at four arbitrarily chosen spots (spot diameter about 1 mm) on the *same* solar cell (sample 601).

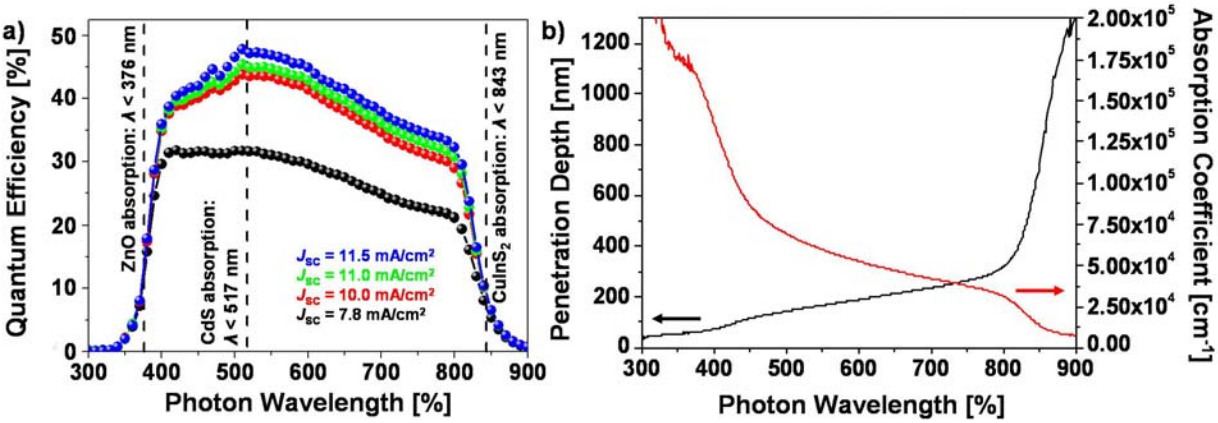

Fig. 6.9: a) External quantum efficiency (*QE*) curves (black, red, green and blue curves) of a solar cell obtained from the Spray ILGAR $CuInS_2$ absorber layer with the smallest thickness of the *well-crystallized top layer* of 178 ± 88 nm (sample 601). The *QE*-curves were recorded at four different spots on the cell (spot diameter: ~1 mm). For each curve, the short-circuit-current-densities J_{SC} were calculated using Eq. (6.6). b) Absorption coefficient α_{abs} (black) and penetration depth ($d_{penetration} = 1/\alpha_{abs}$) of Spray ILGAR $CuInS_2$ as determined from transmittance and reflectance data. The preparation conditions of sample 601 are given in Appendix I.

Even though the shapes of the *QE*-curves agree qualitatively, their maximal *QE*-values vary between QE_{max} = 32 ± 1 % and QE_{max} = 47 ± 1 % for this cell. These variations resulted in variations of the values for J_{SC}, which were calculated from these *QE*-curves using Eq. (6.6) and the AM1.5 solar spectrum (Appendix IX). Thus, values for J_{SC} of 11.5 mA/cm^2 (blue curve), 11.0 mA/cm^2 (green curve), 10.0 mA/cm^2 (red curve) and 7.8 mA/cm^2 (black curve) were determined. From the *JV*-curve of the solar cell an integral value for J_{SC} of 9.6 mA/cm^2 was determined, which lies in between the values obtained from the *QE*-curves. The variation of the J_{SC} values calculated from the *QE*-curves recorded at different spots on the same solar cell, show that the photovoltaic parameters of the device vary locally. Based on the simulated *QE*-curves in Fig. 6.8b, this variation of QE_{max} and J_{SC} may be attributed to the fluctuations of the thickness of the *well-crystallized top layer* of the Spray ILGAR $CuInS_2$ absorber layer (d_{TL} = 178 ± 88 nm).
In order to assess the influence of these thickness fluctuations quantitatively, the absorption coefficient α_{abs} of Spray ILGAR-deposited $CuInS_2$ was determined from transmittance and reflectance spectra of a Spray ILGAR $CuInS_2$ thin film, which was deposited onto a quartz substrate. The obtained absorption coefficient agreed well with absorption data of single-crystalline $CuInS_2$ reported by Neumann *et al.* [Neumann '81]. In Fig. 6.9b, the absorption coefficient of Spray ILGAR $CuInS_2$ and the resulting penetration depth ($d_{penetration} = 1/\alpha_{abs}$) are shown as a function of the photon wavelength.
The strongest decrease of the *QE* is observed for wavelengths, which are larger than about 500-600 nm (Fig. 6.9a). This corresponds to photons, which have a penetration depth greater than about 100-200 nm (Fig. 6.9b) and lies in the same range as the thickness of the *well-crystallized top layer* of the sample 601 (d_{TL} = 178 ± 88 nm). This indicates that only those

charge carriers can be collected in the Spray ILGAR $CuInS_2$-based solar cells that are generated in the *top layer* of the absorber. In contrast, charge carriers, which are generated by photons penetrating so deeply into device that they reach the *layered bottom layer* of the absorber, are likely to recombine due to the high density of defects in this part of the film. Consequently, these charge carriers cannot contribute to the photocurrent and cause a decrease of the *QE*. This behavior also agrees with the influence of a variation of the *top layer* thickness that was predicted by the simulated *QE*-curves in Fig. 6.8b[29].

In the following, the conclusions about the role of the *well-crystallized top layer* and the *layered bottom layer* of the Spray ILGAR $CuInS_2$ absorber layers on the photovoltaic performance of the solar cells, which were analyzed in this section, are summarized.

Influence of the Well-Crystallized Top Layer on the Photovoltaic Performance

The analysis of the *JV*- and *QE*-curves of the Spray ILGAR $CuInS_2$-based solar cells in this section led to the conclusion that the photocurrent of these devices is almost completely generated in the *well-crystallized top layer* of the Spray ILGAR $CuInS_2$ absorber layer. This agrees well with the Raman and SEM analysis of the *well-crystallized top layer* (Fig. 5.14), which showed that it solely consists of chalcopyrite-type $CuInS_2$ with grain sizes of several hundred nanometers. Thus, only electron-hole-pairs, which are *generated and separated* in the *top layer* of the absorber can contribute to the photocurrent of the solar cells. If electron-hole-pairs are generated in the *layered bottom layer*, they are likely to recombine due to the high density of crystalline defects in this part of the absorber. The local fluctuations of the *top layer* thickness, cause local variations of the *QE* and the short-circuit-current-density J_{SC} of the solar cells. However, the electrons of electron-hole-pairs, which have been generated and separated in the *well-crystallized top layer*, have to pass the *layered bottom layer* in order to reach the back contact and to contribute to the photocurrent.

Influence of the Layered Bottom Layer on the Photovoltaic Performance

As shown in sections 4.4.2.4. (Fig. 4.17) and 5.3. (Fig. 5.18) the *layered bottom layer* of the Spray ILGAR $CuInS_2$ absorber layers consists of nanocrystalline $CuInS_2$ and carbon interlayers of nanocrystalline graphite and amorphous carbon. It was further shown, that the nanocrystalline $CuInS_2$ domains in the *layered bottom layer* contain CuAu-ordered and chalcopyrite-type $CuInS_2$ and exhibit an increased degree of disorder compared to the *well-crystallized top layer* (section 5.2.). This defective and disordered structure of the *layered bottom layer* leads to an increased recombination of the charge carriers in the *layered bottom layer*, which prevents their contributuion to the photocurrent of the solar cell.
As indium diffuses out of the *layered bottom layer* during the post-deposition H_2S annealing, conductive paths between its surface and the molybdenum backcontact may be formed by the conductive carbon interlayers. The formation of such paths becomes the more likely the more indium diffuses out of the *bottom layer*, i.e. it increases for an increasing thickness ratio of the *bottom* and *top layer* of the absorber. If the absorber layers are processed to solar cells, these conductive paths may act in two ways:

- They may either facilitate the electron transfer from the *well-crystallized top layer* to the back contact, by bypassing the less conductive nanocrystalline $CuInS_2$ in the *bottom layer*. This process is especially likely, if the *top layer* thickness only shows

[29] An additional loss of charge carriers and thus a reduction of QE_{max} compared to highly efficient RTP $CuInS_2$-based solar cells may result from the increased density of (structural) defects that was observed in the *well-crystallized top layer* of the Spray ILGAR $CuInS_2$ thin film in section 5.4.

small local fluctuations, and may be assumed to account for the low series resistance of the solar cells investigated in this section ($R_{Series} < 2\ \Omega cm^2$).

- Alternatively, the conductive paths may lead to a shunting of the device if they connect the front and back contact of the solar cells. This case is especially likely, if the thickness of the *well-crystallized top layer* shows pronounced local fluctuations or if the *layered bottom layer* exhibits a high density of voids and cracks as they were observed in Sample 604 (Fig. 6.5h). In the case of shunting the conductive paths in the *bottom layer lead* to a degradation of the device.

Similar observations were reported by Kaelin *et al.* [Kaelin '05], who prepared $Cu(In,Ga)Se_2$-based solar cells by doctor-blading consisting of a well-crystallized $Cu(In,Ga)Se_2$ layer on top of a carbon film of several hundred nanometers. These cells reached efficiencies of up to 6.7 % in spite of the presence of the carbon layer. Even though no further investigations about the role of carbon were reported by Kaelin et al, this points towards a similar role of carbon as discussed here.

These influences of the *well-crystallized top layer* and of the *layered bottom layer* indicate that for the optimum performance of Spray ILGAR $CuInS_2$-based solar cells, the absorber preparation must balance between maximizing the crystal quality of the *top layer* and minimizing the risk of shunting in the *bottom layer*. This may be achieved by finely adjusting the nominal absorber layer thickness and the duration of the H_2S step in the ILGAR-cycle. However, since in the Spray ILGAR $CuInS_2$ deposition process, the *well-crystallized top layer* is always formed at the expense of the *layered bottom layer*, the efficiencies of Spray ILGAR $CuInS_2$-based solar cells may be assumed to be limited by the layered morphology of the absorber layer. However, such a balance between the *top* and *bottom layer* properties would not be needed anymore, if the layered morphology of the films could be overcome. Therefore, the addition of H_2O to the spraying solutions, which resulted in Spray ILGAR $CuInS_2$ thin films without a layered morphology (section 4.6.), seems to be a promising process modification in order to further increase the efficiencies of Spray ILGAR $CuInS_2$-based solar cells.

Summary

In conclusion, the results presented in this section, which were obtained from *JV*- and *QE*-measurements of solar cells made from Spray ILGAR $CuInS_2$ absorber layers, showed that working solar cells with efficiencies of up to 4.1 % could be prepared from these films. Furthermore, the influence of the *well-crystallized top layer* and the *layered bottom layer* could be obtained from these measurements. These results were interpreted such that the charge carrier generation and separation in the Spray ILGAR $CuInS_2$-based solar cells mainly occurs in the *well-crystallized top layer* of the absorber layer. In contrast, the thin $CuInS_2$-layers in the *layered bottom layer* of the absorber do not contribute to the generation and collection of charge carriers due to the high defect density in this part of the absorber. The carbon-interlayers found in the *layered bottom layer* of the Spray ILGAR $CuInS_2$ absorbers, provide low-resistivity conduction paths between the *top layer* and the back contact, but also increase the risk of shunting of the device. Therefore, the preparation parameters of the absorber layers have to be finely adjusted in order to obtain a *well-crystallized top layer* of maximum thickness and to simultaneously prevent the creation of shunts in the *layered bottom layer*.